catalysts

MDPI

Article

Construction of Lamellar CoFe-LDHs@MoS_2 to Promote Permonosulfate Properties Leading to Effective Photocatalytic Degradation of Norfloxacin

Tao Wu [1], Xin Ren [1,2,*] and Xuesong Zhao [1,2,*]

[1] College of Engineering, Jilin Normal University, Siping 136000, China; tao20010604@163.com
[2] Key Laboratory of Environmental Materials and Pollution Control, Education Department of Jilin Province, Siping 136000, China
* Correspondence: renxin@jlnu.edu.cn (X.R.); zhaoxuesong008@163.com (X.Z.)

Abstract: The utilization of the photo catalytic activation of permonosulfate (PMS) for the combined breakdown of pollutants has become a focal point in research. Layered double hydroxides (LDHs) have a unique layered structure which is conducive to the adsorption and diffusion of reactants, and can provide more active sites for photocatalytic reactions. The anions between the layers can be exchanged with a variety of substances so that specific catalytically active species can be introduced as needed. LDHs themselves have certain catalytic activity, which can produce synergistic catalysis between LDHs and the supported photocatalytic active substances, and further improve the degradation effect of antibiotics. In actual wastewater treatment, LDHs as a catalyst carrier have a good application prospect. However, the poor activation effect is attributed to the low separation efficiency of catalyst carriers and insufficient active sites. In this study, a dual active site system consisting of Co and Fe, known as CoFe-LDHs@MoS_2, was developed as a catalyst to facilitate the synergistic degradation of norfloxacin (NOF) by PMS under visible light. The findings demonstrate that the material possesses an effective capacity for the synergistic degradation of NOF. A comprehensive investigation was conducted to assess the impact of different catalysts, PMS dosage, degradation systems (Vis, PMS, or Vis PMS), catalyst dosage, NOF concentration, pH, and cycle times on the degradation performance. The active free radicals, degradation pathways, and intermediate toxicity were elucidated through capture experiments, Electron Paramagnetic Resonance Spectrometer (ESR) analysis, a liquid mass spectrometry (LC-MS) toxicity assessment, and theoretical calculations. This research offers a novel approach for designing catalysts with exposed high activity sites for the effective removal of NOF from environmental water.

Keywords: LDHs; PMS; antibiotics; visible light

check for updates

Citation: Wu, T.; Ren, X.; Zhao, X. Construction of Lamellar CoFe-LDHs@MoS_2 to Promote Permonosulfate Properties Leading to Effective Photocatalytic Degradation of Norfloxacin. *Catalysts* **2024**, *14*, 860. https://doi.org/10.3390/catal14120860

Academic Editor: Jae Sung Lee

Received: 17 October 2024
Revised: 17 November 2024
Accepted: 20 November 2024
Published: 26 November 2024

Copyright: © 2024 by the authors. Licensee MDPI, Basel, Switzerland. This article is an open access article distributed under the terms and conditions of the Creative Commons Attribution (CC BY) license (https://creativecommons.org/licenses/by/4.0/).

1. Introduction

Antibiotics, derived from natural or synthetic sources, are indispensable tools in the battle against bacterial infections [1]. They are extensively utilized in medical, agricultural, and animal husbandry settings to combat a diverse array of diseases [2–4]. However, the excessive and indiscriminate use of antibiotics has precipitated the emergence of antibiotic-resistant bacteria, presenting a formidable threat to global public health [5–7]. Furthermore, the widespread utilization of antibiotics has been correlated with ecological degradation [8], exacerbating the risks to both human health and the environment [9]. Consequently, antibiotic resistance stands as one of the top three perils identified by the World Health Organization (WHO).

Layered double hydroxides (LDHs) have high thermal and chemical stability, their structure can remain relatively intact during the repeated cycle of photocatalytic antibiotic degradation, and they will not easily decompose or deform. This makes the catalyst

extremely reusable. In the process of photocatalysis, the separation efficiency of the photogenerated carrier is very important to the catalytic effect. The LDHs' structure can effectively promote the separation of photogenerated carriers. When light is irradiated on the LDHs loaded with photocatalytic active substances, the photogenerated electrons and holes generated can migrate to different directions more efficiently under the guidance of this special structure, reducing the probability of their recombination, thus improving the photocatalytic activity and making the degradation of antibiotics more efficient. It can be combined with other materials to build a composite photocatalyst for the removal of antibiotic contaminants from actual wastewater. And LDHs are reusable, which can reduce the processing cost [10–13].

Norfloxacin (NOF), a member of the second-generation fluorocarbons, is extensively utilized in the management of enteritis, diarrhea, urinary tract infections [14], and various other medical conditions in humans [15]. The existing techniques for eliminating antibiotics from water, such as biodegradation, adsorption, membrane separation, and electrical oxidation, have proven to be only partially effective [6]. Consequently, advanced removal technologies for NOF in aquatic environments have garnered global attention from researchers [16]. Among these technologies, sulfate radical technology stands out due to its safety, non-toxic nature, and superior oxidation potential [14]. Researchers are delving deeply into this technology to devise enhanced approaches for antibiotic removal with the ultimate goal of addressing this critical issue concerning water quality and environmental protection [17]. Remarkable strides are being made in this field and the potential benefits for water treatment are indeed substantial [15].

In the interim, LDHs can serve as a precursor to $SO_4^{-\bullet}$ through peroxymonosulfate (PMS) and permonosulfate (PS), offering an economical and adaptable approach. The activation methods commonly employed encompass photo activation, alkaline activation, thermoplastic, ultrasound irradiation, treatment of transition metal ions, such as Ni, Fe, Mn, and Co, as well as the incorporation of noble metals [18,19]. Utilizing both SRAOPs reaction and photocatalytic reaction in conjunction with transition metals has proven effective in pollutant removal by enabling the complete activation of PMS and efficient degradation [5]. Nevertheless, the widespread application is impeded by the high cost and limited natural abundance of noble metals [20,21]. Transition metal materials such as Ni, Fe, Cu, and Mn, particularly Co-based compounds, demonstrate considerable prowess in activating PMS due to their capability to repeatedly generate $SO_4^{-\bullet}$ during the transformation from Co(II) to Co(III) [21]. Furthermore, Co-based materials come at a lower cost and are more readily available compared to noble metals [22,23]. The micro-structure of the prepared CBMO was comprehensively examined utilizing XRD, SEM, XPS, FT-IR, UV–Vis, and ESR. Meanwhile, the catalytic capacity of the CoFe-LDHs@MoS_2 composite was assessed using sulfate radical-based oxidation and photocatalysis under visible light irradiation for degrading high concentration aqueous NOF.

2. Results and Discussion

2.1. XRD Diffraction

The XRD patterns of the CoFe-LDHs@MoS_2, CoFe-LDHs, and MoS_2 samples are shown in Figure 1A. The peaks observed at 2θ = 11.3°, 22.8°, 34.5°, 60.4°, and 61.7° corresponded to the (003), (006), (009), and (110) planes of CoFe-LDHs [24], which were consistent with PDF No. 3040 reference data. Additionally, the peaks observed at 14.46°, 29.12°, 32.96°, 38.15°, 47.90°, 51.85°, and 58.15° were attributed to the (003), (006), (101), (104), (107), (018), and (110) planes of MoS_2 [24,25]. The XRD pattern of the CoFe-LDHs@MoS_2 sample contained all XRD peaks of CoFe-LDHs and MoS_2, suggesting the successful composite of the two components.

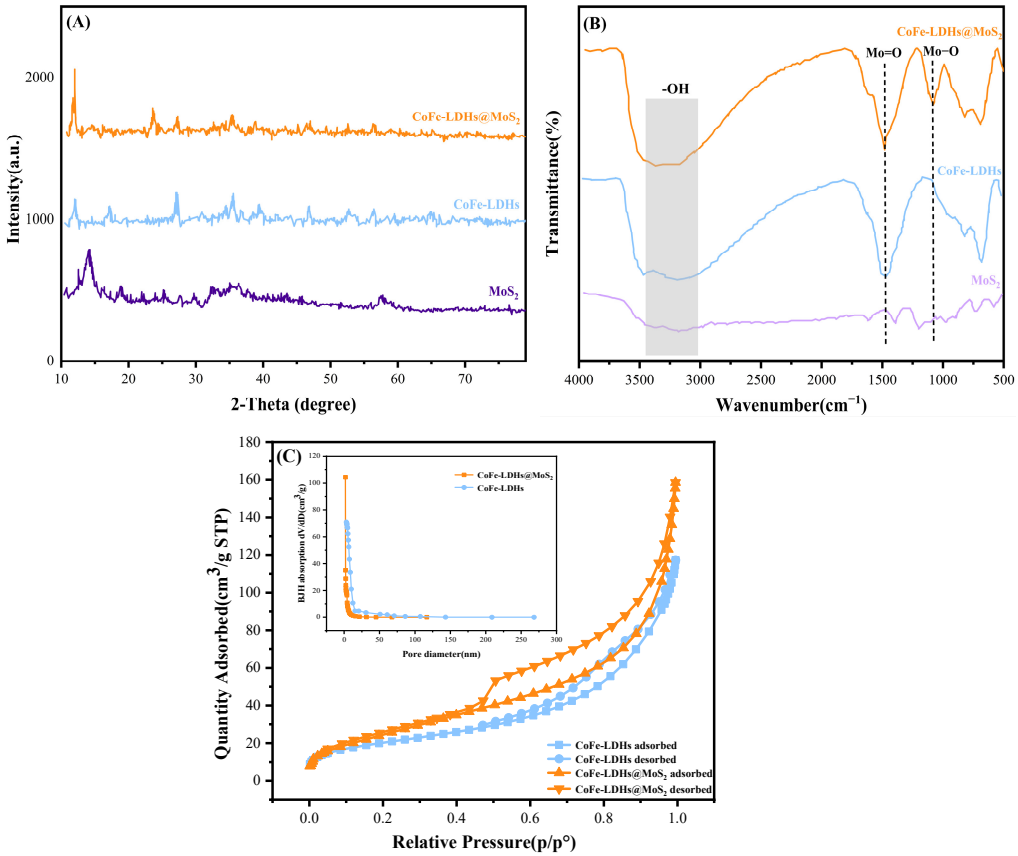

Figure 1. XRD (**A**) and FT-IR (**B**) spectra diffraction of CoFe-LDHs, MoS_2, and CoFe-LDHs@MoS_2; (**C**) CoFe-LDHs and CoFe-LDHs@MoS_2 analysis of nitrogen adsorption before and after use.

Moreover, the FT-IR analysis was further utilized to examine the surface characteristics of the CoFe-LDHs@MoS_2, CoFe-LDHs, and MoS_2 samples. As depicted in Figure 1B, the bands positioned at 3422 cm^{-1} were assigned to the stretching of –OH groups [25]. For the MoS_2 sample, the bands at 484, 904, 950, and 1626 cm^{-1} were associated with the stretching vibration of Mo–S, S–S, Mo–O, and Mo–O [26]. Also, the bands at 698, 825, and 1500 cm^{-1} were ascribed to the Co–O, Fe–O, and C–O stretching vibrations [27]. Furthermore, a new adsorption bond at 1095 cm^{-1} could be attributed to M–Mo stretching vibrations, which was consistent with previous reports [28,29]. As a result, the above-stated investigation findings suggested the successful synthesis of CoFe-LDHs@MoS_2 nanocomposites.

2.2. Scanning Electron Microscope

From the electron microscope image in Figure 2A,B, CoFe-LDHs appears to have a blocky and agglomerated appearance. These blocky structures may have irregular outlines or a shape similar to mica flakes, with edges that are not particularly smooth but rather exhibit a certain degree of curvature and undulation. In the field of view, the CoFe-LDHs are uniformly distributed on the substrate. However, there are also local aggregation phenomena, where certain regions have higher concentrations of hydrated oxides and form more dense clusters, while other regions are relatively sparse. Figure 2C MoS_2 has a ball-shaped, irregular macroscopic appearance. In the field of view, the plate-like structure of molybdenum disulfide may be unevenly distributed due to certain factors during the preparation process, such as the possibility of plate-like structures aggregating in certain regions to form an "island-like" distribution, while other regions are relatively sparse. In Figure 2D,E, the loading of b on a can be observed.

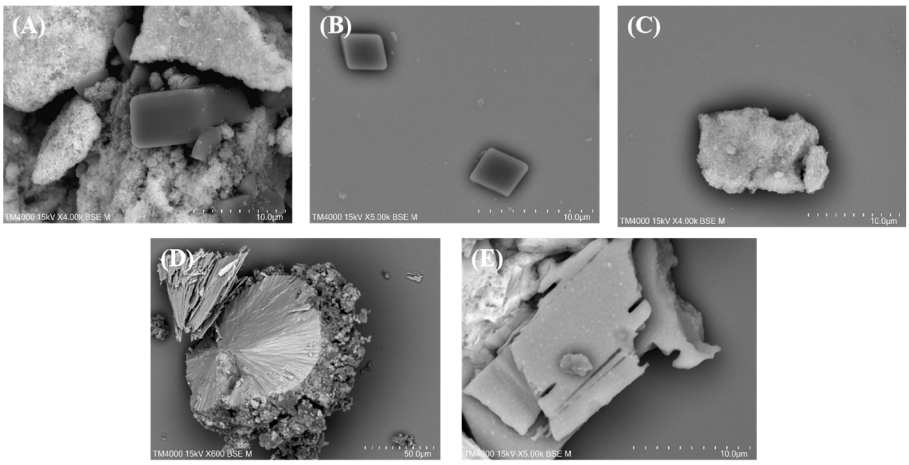

Figure 2. (**A**,**B**) SEM images of CoFe-LDHs samples with different magnification (4000 K and 6000 K), (**C**) MoS_2, (**D**,**E**) CoFe-LDHs@MoS_2 samples with different magnification (600 K and 5000 K).

As depicted in Figure 1C, the nitrogen adsorption analysis indicates that the specific surface area of MoS_2, CoFe-LDHs, and CoFe-LDHs@MoS_2 notably increased. The raised specific surface area of CoFe-LDHs@MoS_2 is advantageous for exposing a greater number of catalytic and adsorption sites, consequently leading to enhanced catalytic degradation performances.

2.3. High-Resolution X-Ray Photo Electron Spectroscopy

As illustrated in Figure 3A, the X-ray photo electron spectroscopy (XPS) full-spectrum analysis confirmed the presence of Fe, O, Mo, S, and Co elements on the surface of the CoFe-LDHs@MoS_2 sample, which was consistent with the results of EDS mapping (Figure 4). The S 2p spectra are depicted in Figure 3B. Two distinct binding energies at 161.6 eV and 162.8 eV were identified as S^{2-} from the $S2p_{2/3}$ and $S2p_{1/3}$ levels within MoS_2 respectively; additionally, a binding energy of 168.9 eV represented SO_4^{2-} due to the partial oxidation of MoS_2 [28]. Furthermore, a binding energy observed at 163.7 eV indicated unsaturated edge sulfur. In Figure 3C, binding energies at 226.1 eV, 228.7 eV, 232.4 eV, and 235.7 eV were associated with S 2s and Mo states, specifically Mo(IV), Mo(IV), and Mo(VI) [26]. The O1s XPS spectrum is also presented in Figure 3D; here, it can be noted that binding energies of both 531.9 eV and 531.0 eV were attributed to lattice oxygen and surface hydroxide groups, respectively [30]. A binding energy of 711.3 eV was attributed to the Fe(II) state (Figure 3E), while a binding energy of 713.6 eV corresponded to the Fe(III) state; this duality is advantageous for facilitating both oxidation and reduction processes involving iron [30–32]. A binding energy of 782.2 eV was assigned to the Co(III) state (Figure 3F), whereas a binding energy of 780.8 eV was ascribed to the Co(II) state [33].

An electrochemical analysis technique was employed to investigate the effective dissociation and transfer of photogenerated charges [34] (Figure 5A). The arrangement of EIS radii was CoFe-LDHs > MoS_2 > CoFe-LDHs@MoS_2, indicating a decrease in the electrochemical impedance during composite formation. The smallest semicircle radius was observed for CoFe-LDHs@MoS_2, confirming its superior kinetics in carrier migration [35]. Moreover, compared to both CoFe-LDHs and MoS_2, the CoFe-LDHs@MoS_2 exhibited a higher transient photocurrent response (Figure 5B), suggesting a more efficient dissociation of carriers [36]. These results are consistent with the EIS tests and further confirm that the CoFe-LDHs@MoS_2 catalyst possesses superior capabilities in the separation and transfer of photogenerated charges [16,17].

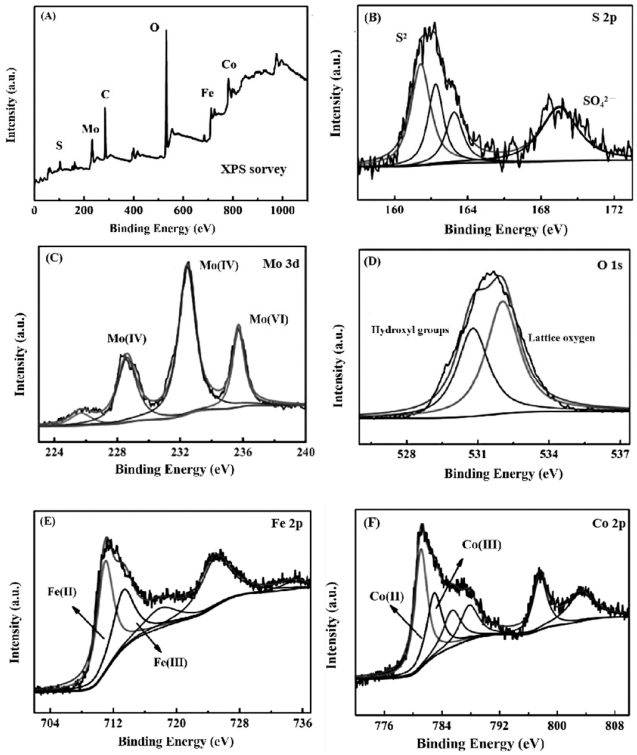

Figure 3. XPS spectra of fresh CoFe-LDHs@MoS_2. (**A**) Survey scan; (**B**) S 2p; (**C**) Mo 3d, (**D**) O 1s, (**E**) Fe 2p, and (**F**) Co 2p.

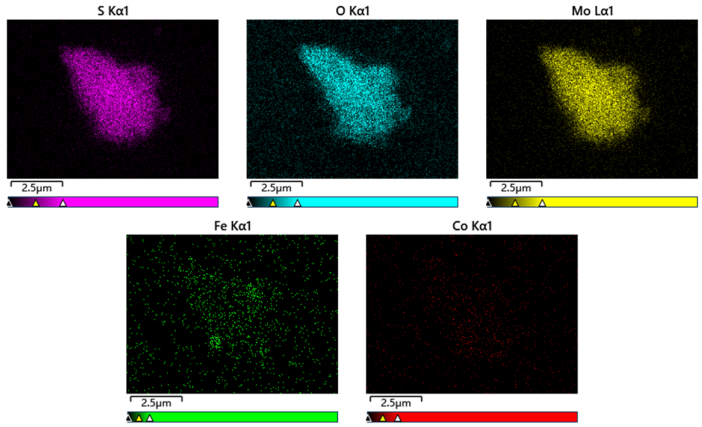

Figure 4. EDS spectra of CoFe-LDHs@MoS_2.

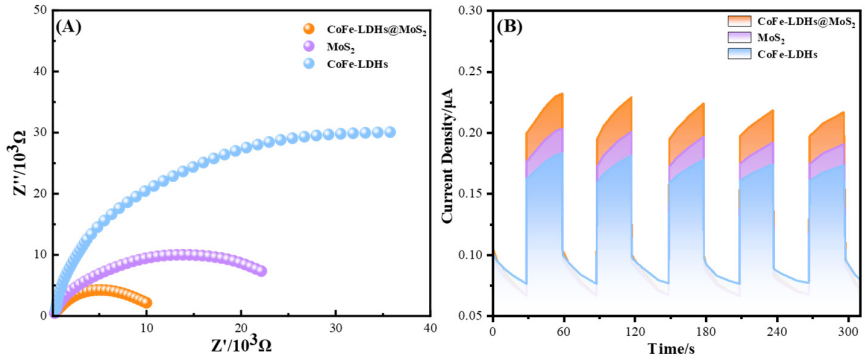

Figure 5. The EIS spectra (**A**) and transient photocurrent response (**B**) curves of CoFe-LDHs, MoS_2, and CoFe-LDHs@MoS_2.

2.4. The Influence of Different Conditions on the Experiment

The results varied significantly under the effect of different conditions, e.g., catalyst types, PMS dosage, and Vis on degradation rate were all investigated. As shown in Figure 6, the degradation rates of the reaction were 0.1%, 12.33%, 31.23%, 43.10%, 45.53%, 62.34%, 64.93%, 66.55%, 71.28%, 83.55%, and 98.81% from top to bottom, respectively, in ascending order. It can be inferred from this that the optimal reaction conditions are CoFe-LDHs@MoS_2 +Vis + PMS.

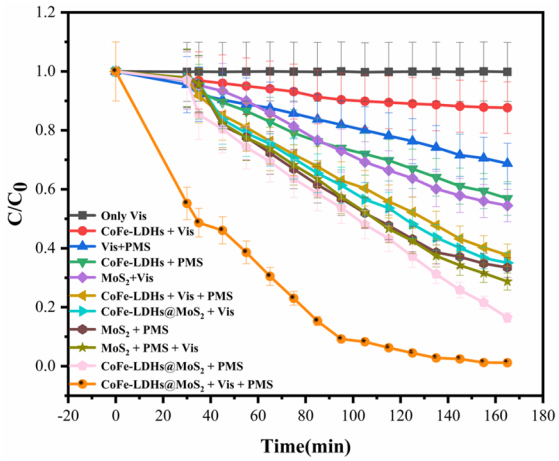

Figure 6. Comparison of catalytic performance.

We first investigated the adsorption performance and catalytic activity of CoFe-LDHs@MoS_2 on NOF in a photo-stimulated PMS system (see Figure 6). Figure 7 depicts the impact of varying quantities of catalysts on the reaction system, while keeping other conditions constant. As depicted in Figure 7A, the degradation efficiency was 95.51% when 0.05 g of catalyst was added, 98.81% when 0.1 g of catalyst was added, and 99.16% when 0.2 g of catalyst was added. It can be observed that as the amount of catalyst added increases, the degradation efficiency of the reaction also accelerates. However, in an effort to conserve resources and minimize environmental impact, we limited the catalyst content to 0.1 g. Figure 7B illustrates the impact of varying concentrations of NOF on the degradation reaction, while keeping all other conditions constant. When NOF = 10 mg L^{-1}, the degradation efficiency was 99.38%; when NOF = 15 mg L^{-1}, the degradation efficiency was 99.14%; when NOF = 20 mg L^{-1}, the degradation efficiency was 98.81%; when NOF = 25 mg L^{-1}, the degradation efficiency was 93.27%; and with an NOF concentration of 10 mg/L, the degradation efficiency was 99.38%. With an increase in NOF to 15 mg L^{-1}, the degradation efficiency decreased slightly to 99.14%. Further increasing the NOF to 20 mg L^{-1} resulted in a reduction in the degradation efficiency to 98.81%. However, when the concentration of NOF reached 25 mg L^{-1}, there was a significant decrease in degradation efficiency to only 93.27%, and at a level of 30 mg L^{-1}, the degradation efficiency further declined to 90.68%. An NOF concentration of 30 mg/L resulted in a degradation efficiency of 90.68%. From this, we can infer that as the concentration of NOF increases, the efficiency of degradation decreases. Excessive NOF may lead to an increase in the molecular weight within the reaction system. This increase in molecular weight has the potential to enhance the generation of active free radicals, as a result of the competition between equal amounts of catalyst and PMS reaction. Consequently, this could lead to a decrease in the reaction rate. Figure 7C illustrates the effect of varying concentrations of PMS on the reaction, while keeping all other conditions constant. When the concentration of PMS was 0.1 mM, the efficiency of degradation reached an impressive 98.81%. As the concentration increased to 0.2 mM, the degradation efficiency remained high at 96.53%. Further increasing the PMS concentration to 0.3 mM still demonstrated a notable degradation efficiency of 94.64%. Even at a higher concentration of 0.4 mM, the degradation efficiency maintained a commendable level at 92.16%. Finally, when the PMS concentration reached 0.5 mM, there was still a considerable

degradation efficiency of 89.61%. As the quantity of PMS added escalated, there was a gradual decrease in the degradation rate of the reaction. Excessive PMS hinders the reaction of the degradation system rather than promoting it, leading to a reduction in its effectiveness. This may be attributed to the fact that the optimal PMS concentration is 0.1 mM. Figure 7D illustrates the impact of varying pH levels on the degradation reaction, while keeping other conditions unchanged. At a pH of 3, the degradation efficiency reached an impressive 99.41%. Similarly, at a pH of 5, the degradation efficiency remained high at 99.15%, showcasing the remarkable performance of the catalyst. Even at neutral conditions with a pH of 7, the degradation efficiency still impressed at 98.81%. Moving towards alkaline conditions, at a pH of 9 and 11, the degradation efficiencies were recorded at respectable levels of 94.45% and 92.16%, respectively. This comprehensive analysis indicates that the catalyst displays exceptional degradation efficiency over a broad pH range from acidic to slightly alkaline conditions (pH 3–11), thus affirming its robust applicability across diverse environmental settings. The decreased efficiency of degradation under strong alkaline conditions, as compared to weak acid and neutral conditions, may be attributed to the excessive reaction between OH- and SO_4^-. This leads to a significant quenching reaction of ·OH, resulting in a reduction in active species and a lower degradation rate under strong alkaline conditions than the others.

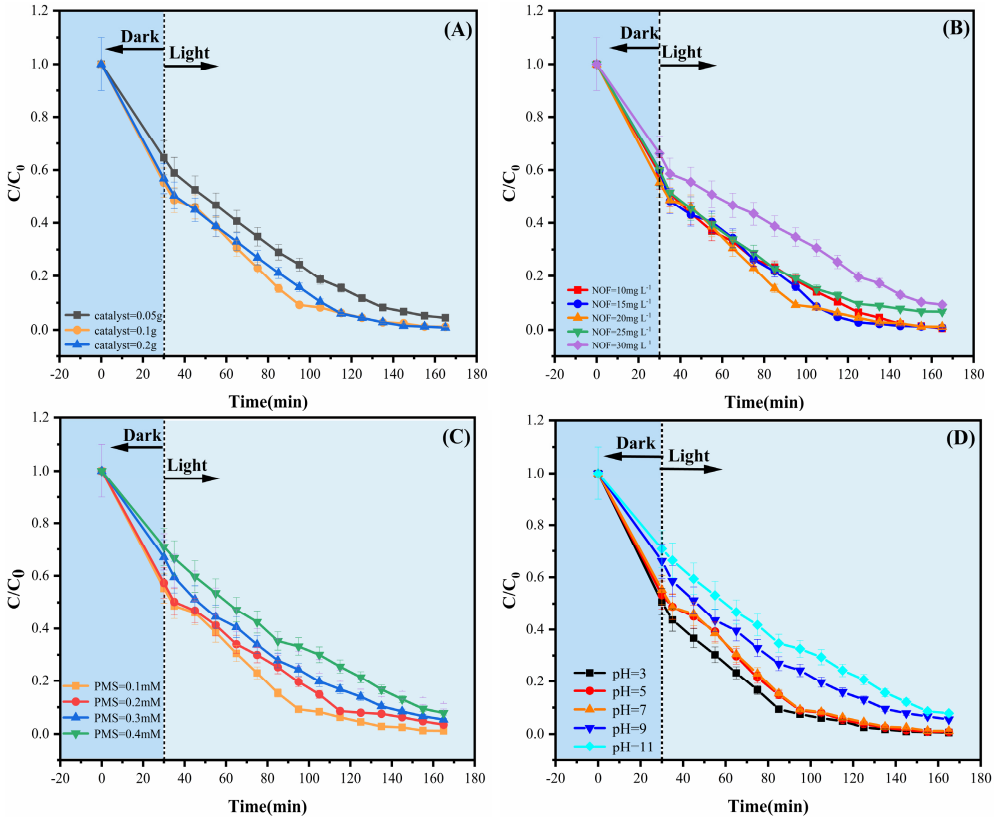

Figure 7. Catalytic performance investigation via control variable method. (**A**) Degradation efficiency of different doses of CoFe-LDHs@MoS_2. (**B**) Degradation efficiency at different levels of NOF. (**C**) Degradation efficiency with different doses of PMS. (**D**) Degradation efficiency at different pH values.

2.5. Analysis of Active Species

Electron Spin Resonance Spectroscopy (ESR) was utilized to analyze the presence of free radicals in the photocatalytic system on Vis CoFe-LDHs@MoS_2, yielding the results depicted in Figure 8A,B. Without light conditions, no detectable active substance signals were observed. However, once exposed to illumination, the generation of free radicals ·OH, $\cdot O_2^-$, and $\cdot SO_4^-$ was evident. Further exploration is necessary to determine

the involvement of free radicals in the degradation of NOF by CoFe-LDHs@MoS_2 [14]. Quenching experiments were conducted on the catalyst, and the findings are illustrated in Figure 8C. We employed chemical substances to seize one or more free radicals in order to monitor the degradation of NOF, while simultaneously ensuring the absence of any other influencing factors. When selecting a reagent for ·OH, methanol or tert butanol is generally preferred [16]. Methanol has a strong trapping effect on $\cdot SO_4^-$, while tert butane exhibits stronger selectivity and excellent binding with ·OH. Henceforth, tert butane was selected as the agent for capturing ·OH, and tert butanol (TBA) was employed specifically for the capture of ·OH. We utilized potassium biodata (1 mM) to capture photogenerated electrons and effectively quench $\cdot O_2^-$, while employing methanol (MeOH) to suppress sulfate radicals ($\cdot SO_4^-$) and hydroxide radicals (·OH). This approach facilitated the meticulous management of reactive oxygen species, ensuring their controlled impact on the system. The findings indicated that the introduction of different capture agents resulted in variable degrees of degradation of NOF, thus further suggesting the involvement of $\cdot O_2^-$, ·OH, and $\cdot SO_4^-$ in the decomposition process of NOF [35]. Following the addition of potassium biodata, there was a notable reduction of 19.93% in the degradation activity of superoxide radicals. After the introduction of methanol, there was a further decrease in degradation performance, reaching 68.18%. The difference in activity following the addition of TBA was in the participation of $\cdot SO_4^-$ in the degradation process, accounting for approximately 44.64% of the reaction [14].

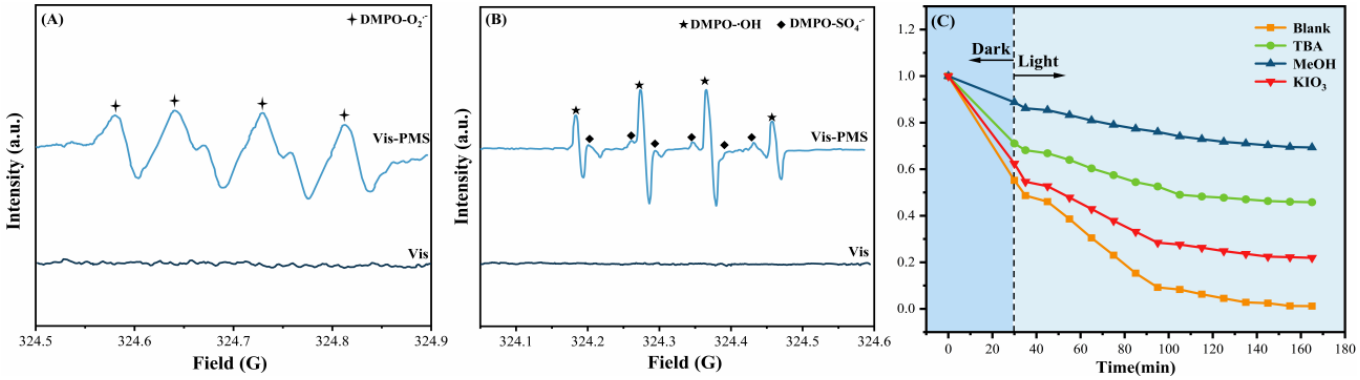

Figure 8. ESR spectra of (**A**) $O_2^{\bullet-}$ and (**B**) ·OH and $SO_4^{\bullet-}$ radical capture experiments (**C**).

2.6. Possible Mechanism Analysis

Catalysts activate PMS to initiate the release of Fe^{2+} and Co^{2+} (Figure 9). Subsequently, Fe^{2+} serves to further activate PMS, leading to the generation of SO_4^-. Concurrently, Fe^{2+} undergoes oxidation, resulting in the production of Fe^{3+}. The metal ions will initially capture and absorb H_2O molecules, resulting in the formation of $CoOH^+$ and $FeOH^{2+}$. This process ultimately leads to the reaction of HSO_5^- to produce SO_4^- and CoO^+. Furthermore, Co^{2+} will react with $FeOH^{2+}$ to yield $CoOH^+$, while the surface of the HSO_5 adsorbent material becomes covered by $CoOH^+$, leading to the generation of SO_4^-. The CoO^+ that is produced undergoes further conversion into Co^{3+}, which in turn serves to activate PMS for the generation of SO_5^-. Trivalent and divalent iron ions also play a role in the production of SO_4^- and SO_5^-. This process forms a cyclic mechanism aimed at achieving ion regeneration [14,37].

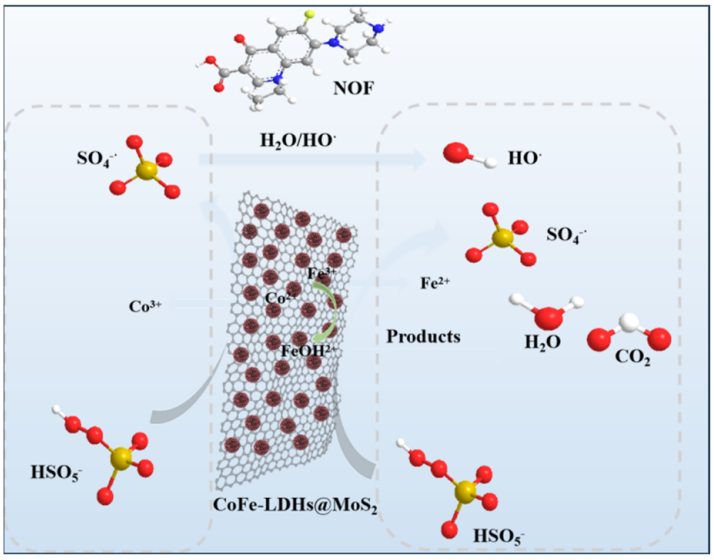

Figure 9. The mechanism analysis diagram.

2.7. Degradation Pathways and Intermediates

Theoretical calculations for norfloxacin are depicted in Figure 10, revealing that atoms with a higher OW-f^0 value in Figure 10A exhibit a relatively heightened susceptibility to attack by free radicals. The benzene and piperazine rings possess regions of elevated electron density that render them prone to electroscopic assault, while the quinolone ring harbors sites susceptible to nucleophilic attack. Based on these theoretical calculations, potential degradation pathways of NOF can be categorized as pipeline ring conversion, deflationary, declaration, and quintillion-based conversion characterized by triphosphate methods.

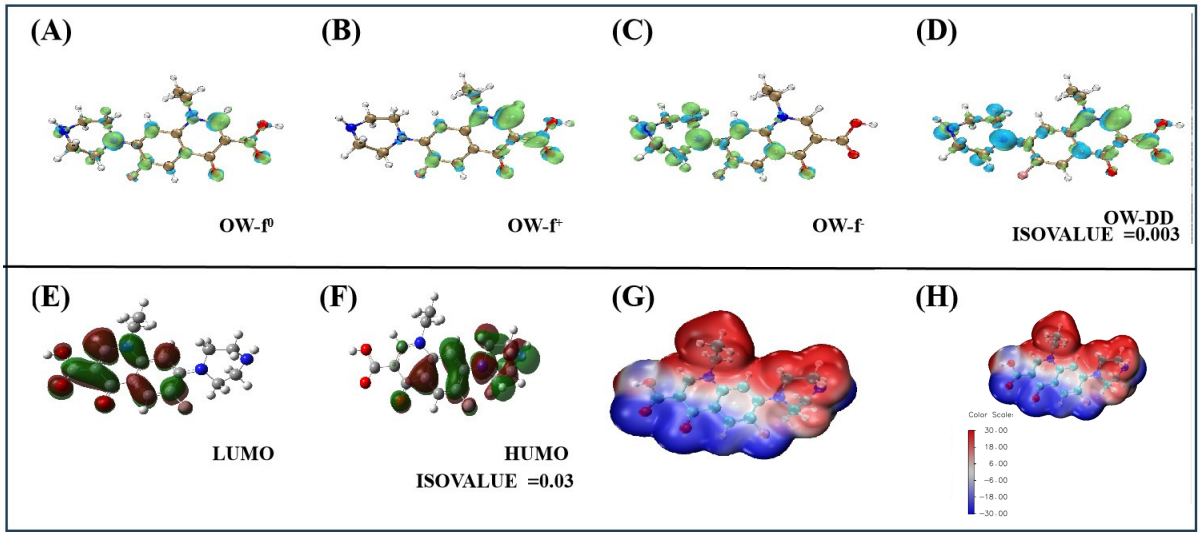

Figure 10. (**A**) OW-f^0, (**B**) OW-f^+, (**C**) OW-f^-, (**D**) CDD of NOF, (**E**) LUMO, (**F**) HUMO, (**G**) optimized NOF structure at the B3LYP/6-31G* level, and (**H**) ESP of SMX.

To elucidate the role of NOF in CoFe-LDHs@MoS_2-Vis-PMS, we conducted a further investigation into the degradation mechanism of NOF intermediates within the system, utilizing an LC-MS methodology. Meanwhile, within (Figure 11) Path 1, NOF underwent decomposition through the declaration of the carboxyl group located on the naphthalene ring, leading to the formation of an intermediate labeled F1 with a mass-to-charge ratio of 307 (m/z = 307). Furthermore, following the ring-opening of the pipeline ring in F1, three

distinct structures emerged, yielding (Figure 11) F2 (m/z = 297), F3 (m/z = 271), and F5 (m/z = 224) [38,39]. In Path 3 (Figure 11), the C-H bond of the pipeline ring or quinolone group was targeted by $SO_4^{-\bullet}$ in NOF, leading to oxidation and an exceedingly unstable state of NOF with subsequent hydroxylation. This process results in the formation of a highly reactive and precarious oxidation state within the NOF compound. Eventually, after undergoing a series of complex transformations and the breaking of chemical bonds, the resultant product F10 emerged.

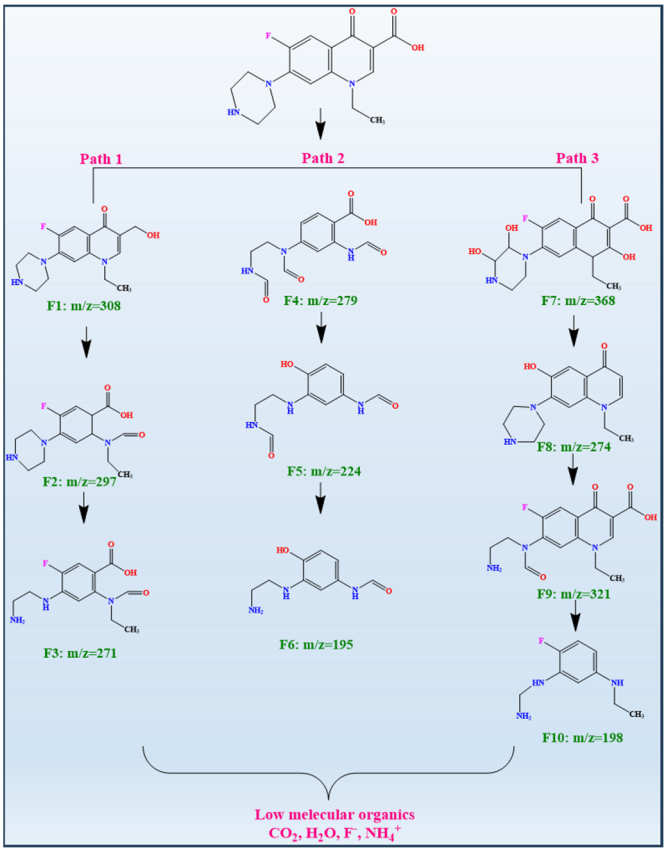

Figure 11. Possible degradation pathways and intermediate products.

The toxicity of NOF and its degradation intermediates was assessed utilizing toxicity evaluation software (TEST) to determine their potential impact on the environment. The Fathead minnow LC50 of NOF (Figure 12A) was recorded at 1.45 mol kg^{-1}, indicating a significant level of toxicity. Furthermore, the LC50 values of all SMX intermediates exhibited an increase, suggesting a noteworthy reduction in their acute toxicity levels. In contrast, with the exception of F1, F8, and F10, all NOF intermediates demonstrated a decrease in their mutagenicity values, indicating a reduction in their mutagenic toxicity. Meanwhile, the mutagenic toxicity of all remaining NOF intermediates experienced a decline. In contrast to F4 and F8, the developmental toxicity of all intermediate products was found to be lower than that of NOF. Interestingly, the bioaccumulation factors for degrading intermediates were observed to be lower than those of NOF, indicating a reduced level of toxicity in all intermediates compared to that of NOF. The CoFe-LDHs@MoS_2-Vis-PMS system represents an efficient and environmentally sustainable approach for the degradation of NOF, showcasing its prowess in the realm of environmental remediation [24].

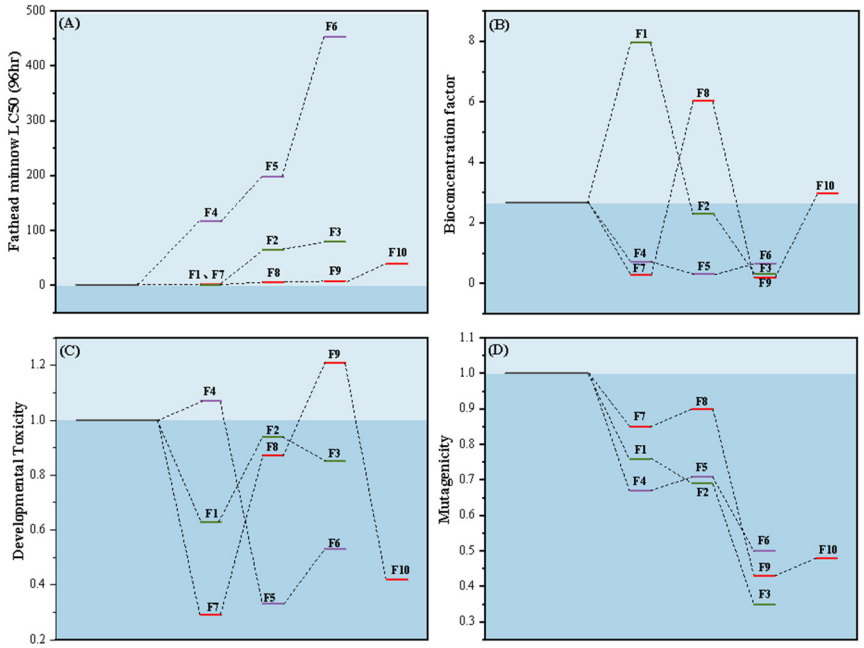

Figure 12. Toxicity evaluation of photo degradation intermediates via TEST, Fathead minnow LC50 (96 h) (**A**), bioaccumulation factor (**B**), developmental toxicity (**C**), and mutagenicity (**D**).

2.8. Catalyst Recovery Experiment

XRD (Figure 13A) and FT-IR (Figure 13B) images of the recovered CoFe-LDHs@MoS_2 show a good crystal structure and morphology, indicating that the prepared catalyst had special suitability and stability. This cyclic experiment was carried out under the most optimal conditions, as illustrated in Figure 13. Following five consecutive trials, the degradation efficiency of the system declined from 98.81% to 89.76% (Figure 13C). This serves as evidence that the system possesses the capability to repeatedly reduce pollutants to a certain extent, thereby substantiating the catalyst's value for recycling and reuse.

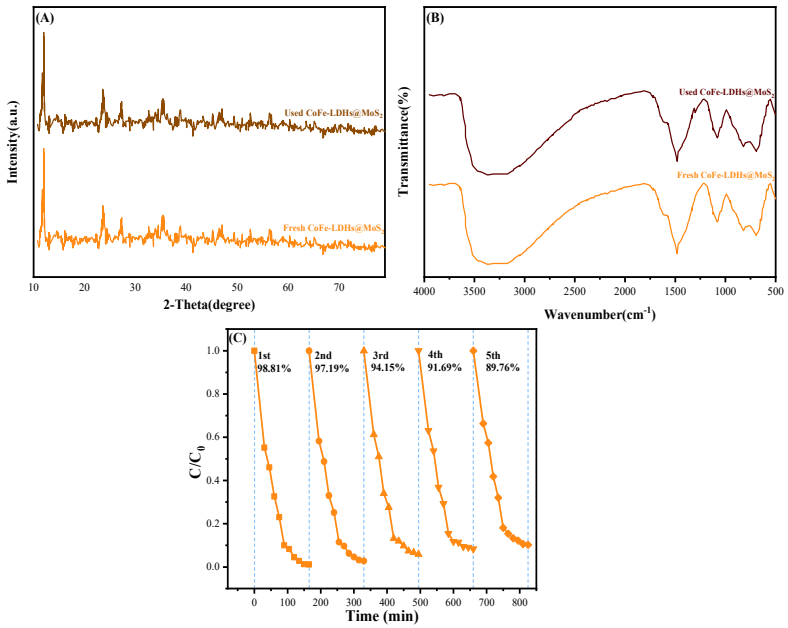

Figure 13. (**A**) XRD diffractograms of fresh CoFe-LDHs@MoS_2 and used CoFe-LDHs@MoS_2, (**B**) Fourier transform infrared spectrum of fresh CoFe-LDHs@MoS_2 and used CoFe-LDHs@MoS_2, (**C**) cycling degradation performance of CoFe-LDHs@MoS_2.

3. Experimental

3.1. Reagents and Materials

All experiments were carried out using ultra-pure water made in the laboratory. $Fe(NO_3)_3 \cdot 9H_2O$ and $Co(NO_3)_2 \cdot 6H_2O$ were purchased from McLean Reagents Ltd. (Ratchasima, Thailand). CH_3OH, C_2H_5OH, and rambutan were purchased from Sinopharm Chemical Reagent Co. (Shanghai, China). Urea and NH_4F were purchased from Wanwei Corporation (Chaohu, China), while tetracycline hydrochloride, $(NH_4)_6Mo_7O_{24} \cdot 4H_2O$, NaOH and potassium biodata were purchased from Aladdin Ltd. (Shanghai, China). All reagents were analytically pure and were not further purified prior to use.

3.2. Preparation of the Catalyst

3.2.1. Preparation of CoFe-LDHs

The CoFe-LDHs were prepared as follows: 4 mmol of $Co(NO_3)_2 \cdot 6H_2O$ and 2 mmol of $Fe(NO_3)_3 \cdot 9H_2O$ were dissolved into 50 mL of water and stirred magnetically for 30 min to form a homogeneous solution. Afterwards, 15 mmol of NH_4F was added and stirred for another 30 min to make the mixture homogeneous and this was recorded as solution A. Meanwhile, 21 mmol of NaOH and 3 mmol of Na_2CO_3 were dissolved into 50 mL of distilled water and recorded as solution B. At last, solution B was added drop by drop to solution A with continuous stirring, and the pH was adjusted to 9.5 with stirring for another 5 h to obtain CoFe-LDHs.

3.2.2. Preparation of CoFe-LDHs@MoS_2

Firstly (Figure 14), 0.3 g of pre-synthesized CoFe-LDHs powder was dispersed in 120 mL of distilled water. Then, 0.45 g of $Na_2MoO_4 \cdot 2H_2O$ and 0.28 g of thioacetamide were added into the above solution and stirring continued for 30 min. Following that, the mixture was placed into a Teflon-lined stainless steel autoclave and heated at 160 °C for 12 h. Finally, the black precipitates were filtered and washed using decolonized water and absolute alcohol three times. After drying in vacuum oven at 60 °C for several hours, the CoFe-LDHs@MoS_2 was obtained. PMS was acquired from Sigma-Aldrich® (St. Louis, MO, USA), and other reagents were purchased from Sinopharm Chemical Reagent Co., Ltd., China. All of these reagents were of analytical grade and used as received without further purification. Double-distilled water was used in all the experiments.

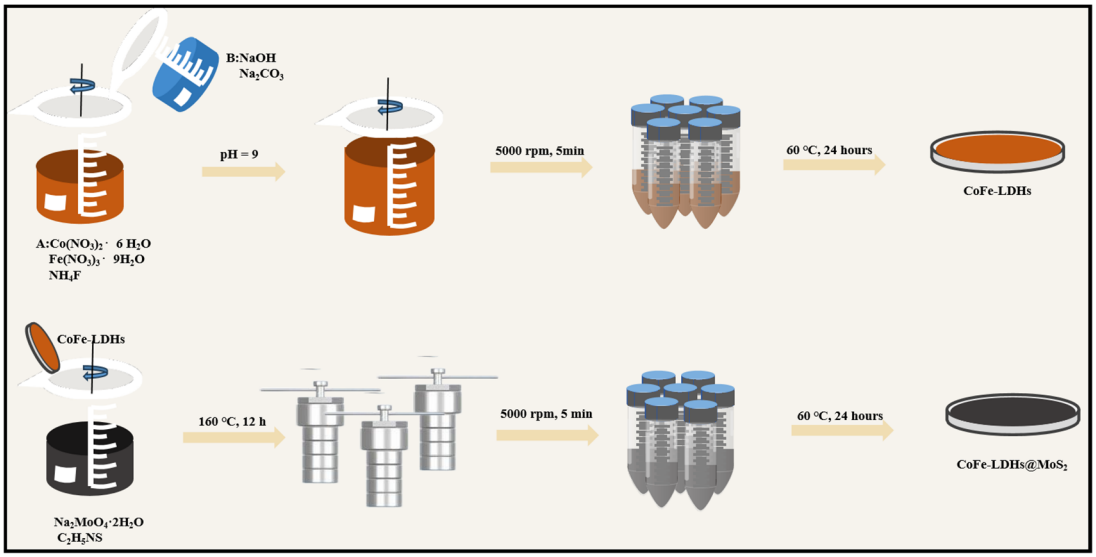

Figure 14. The catalyst process preparation diagram.

3.3. Experimental Instruments and Test Parameters

XRD test machine Equipment: Bruker (Billerica, MA, USA) D8 ADVANCE, test conditions angle 5~60°, the Scanning speed is 5 °C/min.

XPS analysis equipment model: ThermoScientific (Waltham, MA, USA) Escalab 250Xi, using AI Ka target (hv = 1486.6 eV), power 150 W, sensitivity 350 keps, analysis chamber vacuum 10^{-8} mbar. The angle between the detector and the sample surface is 90°, and the analysis area is 700 × 300 μm.

BET analysis equipment model: ASAP 2020 specific surface and porosity analyzer (Micromeritics, Norcross, GA, USA); test conditions are conventional conditions.

EIS uses an electrochemical workstation (model: Shanghai Chenhua (Shanghai, China) CHI760E). The test adopts a three-electrode system, saturated calomel electrode (SCE) as the reference electrode (RE), the auxiliary electrode (CE) uses platinum electrode, and the sample is the working electrode.

EPR test instrument: EPR 5000 [11-0521] (Kansas, MI, USA). Test parameters: filter parameter: 0.1; filter type: DIG; frequency: 9; non-marker amplitude: 108; phase angle: 0; Q-factor: 1600; NL: 47; temperature: 28.5.

The computational calculations based on density functional theory (DFT) were carried out with Gaussian 16C.01 program package. The geometry optimization and single-point energy calculations were executed with B3LYP-D3(BJ) theoretical method using 6-31G(d) basis set to generate electronic wave functions and structure coordinates of NOF.

Liquid Chromatograph Mass Spectrometer (LCMS), Agilent 1260 (Santa Clara, CA, USA). Test Parameters: chromatographic column: X Bridge C18 (50 mm × 4.6 mm × 5 μm); flow phase: methanol 95%–pure water 5%; flowrate: 0.4 mL/min; injection volume: 20 μL; ion source: ESI DAD detector, positive ion mode, 200~600 nm full scan ESI ion source, positive ion mode, scanning range: m/z 100~1400; capillary voltage: 3.8 kV; spray pressure: 60 psi.

4. Conclusions

This article explores the fabrication of CoFe-LDHs@MoS_2 catalysts with sheet-like structures. With its superior crystallinity and unique sheet-like morphology, CoFe-LDHs@MoS_2 demonstrates exceptional catalytic performance for NOF. Moreover, it exhibits a synergistic effect between visible light and PMS, thereby highlighting the effectiveness and repeatability of CoFe-LDHs@MoS_2 as a catalyst. Through the activation of PMS under the irradiation of visible light, a remarkable degradation rate of 98.81% for NOF can be achieved within the timespan of 165 min. Furthermore, experiments on quenching and EPR detection have demonstrated that within the CoFe-LDHs@MoS_2-vis-PMS system, $\cdot O_2^-$, $\cdot OH^-$, and $\cdot SO_4^-$ are the primary reactive free radicals responsible for the degradation of NOF. Furthermore, the primary degradation pathways of NOF encompass pipeline ring conversion, deflationary, declaration, and quintillion group conversion. In conclusion, the CoFe-LDHs@MoS_2-Vis-PMS system demonstrates remarkable efficacy in eliminating persistent antibiotics from wastewater and is poised to cater to the exigencies of future environmental water pollution treatment.

Author Contributions: Conceptualization, X.Z.; formal analysis, investigation, and writing—original draft, T.W.; writing—review and editing, X.R. All authors have read and agreed to the published version of the manuscript.

Funding: This project was supported by grants from the Natural Science Foundation of Jilin Province (20230101220JC).

Data Availability Statement: All data are present within the manuscript.

Conflicts of Interest: The authors declare no conflicts of interest.

References

1. Li, L.; Xu, H.; Qian, Z.; Zhan, Z.; Liang, X.; Xing, J. Estimation methods of wetland carbon sink and factors infuencing wetland carbon cycle: A review. *Carbon Res.* **2024**, *3*, 50. [CrossRef]
2. Li, L.; Liang, T.; Zhao, M.; Lv, Y.; Song, Z.; Sheng, T.; Ma, F. A review on mycelial pellets as biological carriers: Wastewater treatment and recovery for resource and energy. *Bioresour. Technol.* **2022**, *355*, 127200. [CrossRef] [PubMed]
3. Li, L.; Chai, W.; Sun, C.; Huang, L.; Sheng, T.; Song, Z.; Fang, M. Role of microalgae-bacterial consortium in wastewater treatment: A review. *J. Environ. Manag.* **2024**, *360*, 121226. [CrossRef]
4. Li, L.; Han, J.; Huang, X.; Qiu, S.; Liu, X.; Liu, L.; Zhao, M.; Qu, J.; Zou, J.; Zhang, J. Organic pollutants removal from aqueous solutions using metal-organic frameworks (MOFs) as adsorbents: A review. *J. Environ. Chem. Eng.* **2023**, *11*, 111217. [CrossRef]
5. Chen, X.; Zhou, J.; Zhang, T.; Ding, L. Enhanced degradation of tetracycline hydrochloride using photocatalysis and sulfate radical-based oxidation processes by Co/$BiVO_4$ composites. *J. Water Process Eng.* **2019**, *32*, 100918. [CrossRef]
6. Sabri, N.; Schmitt, H.; Vander, B.; Gerritsen, H.; Zuidema, T.; Rijnaarts, H.; Lan, A. Prevalence of antibiotics and antibiotic resistance genes in a wastewater effluent-receiving river in the Netherland. *J. Environ. Chem. Eng.* **2018**, *8*, 102245. [CrossRef]
7. Singh, R.; Singh, A.P.; Kumar, S.; Giri, B.S.; Kim, K.-H. Antibiotic resistance in major rivers in the world: A systematic review on occurrence, emergence, and management strategies. *J. Clean. Prod.* **2019**, *234*, 1484–1505. [CrossRef]
8. Chen, Y.; Zhang, G.; Liu, H.; Qu, J. Confining Free Radicals in Close Vicinity to Contaminants Enables Ultrafast Fenton-like Processes in the Interspacing of MoS_2 Membranes. *Angew. Chem. (Int. Ed. Engl.)* **2019**, *58*, 8134–8138. [CrossRef]
9. Zheng, X.; Xu, J.; Yan, K.; Wang, H.; Wang, Z.; Yang, S. Space-Confined Growth of MoS_2 Nanosheets within Graphite: The Layered Hybrid of MoS_2 and Graphene as an Active Catalyst for Hydrogen Evolution Reaction. *Chem. Mater.* **2014**, *26*, 2344–2353. [CrossRef]
10. Sun, Q.; Zhao, Y.; Zhang, J.; Sheng, J. Efficient degradation of antibiotics over Co(II)-doped Bi_2MoO_6 nanohybrid via the synergy of peroxymonosulfate activation and photocatalytic reaction under visible irradiation. *Chemosphere* **2022**, *320*, 134807. [CrossRef]
11. Zeng, H.; Zhu, H.; Deng, J.; Shi, Z.; Zhang, H.; Li, X.; Deng, L. New insight into peroxymonosulfate activation by CoAl-LDH derived CoOOH: Oxygen vacancies rather than Co species redox pairs induced process. *Chem. Eng. J.* **2022**, *442*, 136251. [CrossRef]
12. Fu, M.; Chai, B.; Zhang, X.; Sun, Y.; Fan, G.; Song, G. Nitrogen self-doped chitosan carbon aerogel integrating with CoAl-LDH for ultra-efficient sulfamethoxazole degradation based on PS-AOPs: From batch to continuous process. *J. Environ. Chem. Eng.* **2023**, *11*, 110650. [CrossRef]
13. Zhu, J.; Zhu, Y.; Zhou, W. Cu-doped Ni-LDH with abundant oxygen vacancies for enhanced methyl 4-hydroxybenzoate degradation via peroxymonosulfate activation: Key role of superoxide radicals. *J. Colloid. Interf. Sci.* **2022**, *610*, 504–517. [CrossRef]
14. Liu, Y.; Liu, W.; Gan, X.; Shang, J.; Cheng, X. High-performance, stable CoNi LDH@Ni foam composite membrane with innovative peroxymonosulfate activation for 2,4-dichlorophenol destruction. *J. Environ. Sci.* **2024**, *141*, 235–248. [CrossRef]
15. Ben, Y.; Fu, C.; Hu, M.; Liu, L.; Wong, M.H.; Zheng, C. Human health risk assessment of antibiotic resistance associated with antibiotic residues in the environment: A review. *Environ. Res.* **2019**, *169*, 483–493. [CrossRef]
16. Huang, Z.; Li, W.; Jiang, J.; Zhou, W.; Zhang, M.; Mao, R.; Wang, Z.; Xie, J.; Hu, Z. Cerium oxide boosted CoFe-N codoped carbon nanotubes with abundant oxygen-vacancies toward efficient oxygen reduction and methanol oxidation reaction. *J. Colloid Interface Sci.* **2024**, *654*, 164–173. [CrossRef]
17. Wu, Y.; Chen, L.; Han, Y.; Liu, P.; Xu, H.; Yu, G.; Wang, Y.; Wen, T.; Ju, W.; Gu, J. Hierarchical construction of CNT networks in aramid papers for high-efficiency microwave absorption. *Nano Res.* **2023**, *16*, 7801–7809. [CrossRef]
18. Zhu, T.T.; Su, Z.X.; Lai, W.X.; Zhang, Y.B.; Liu, Y.W. Insights into the fate and removal of antibiotics and antibiotic resistance genes using biological wastewater treatment technology. *Sci. Total Environ.* **2021**, *776*, 145906. [CrossRef]
19. Luo, H.; Xiao, P.; Hong, W. Dielectric behavior of laminate-structure Cf/Si_3N_4 composites in X-band. *Appl. Phys. Lett.* **2014**, *105*, 172903. [CrossRef]
20. Liang, B.; Wang, S.; Kuang, D.; Hou, L.; Yu, B.; Lin, L.; Deng, L.; Huang, H.; He, J. Facile synthesis and excellent microwave absorption properties of FeCo-C core–shell nanoparticles. *Nanotechnology* **2018**, *29*, 085604. [CrossRef]
21. Silambarasan, K.; Archana, J.; Harish, S.; Navaneethan, M.; Sankar, R.; Ponnusamy, S.; Muth, C. One-step fabrication of ultrathin layered 1T@2H phase MoS_2 with high catalytic activity based counter electrode for photovoltaic devices. *J. Mater. Sci. Technol.* **2020**, *51*, 94–101.
22. Liu, H.; Wei, G.; Xu, Z.; Liu, P.; Li, Y. Quantitative analysis of Fe and Co in Co-substituted magnetite using XPS: The application of non-linear least squares fitting (NLLSF). *Appl. Surf. Sci.* **2016**, *389*, 438–446. [CrossRef]
23. Chen, M.; Chu, W. Efficient Degradation of an Antibiotic Norfloxacin in Aqueous Solution via a Simulated Solar-Light-Mediated Bi_2WO_6 Process. *Ind. Eng. Chem. Res.* **2012**, *51*, 4887–4893. [CrossRef]
24. Li, J.; Cao, H.; Qi, H.; Li, Y.; Zhu, S.; Ye, X.; Zhang, J.; Yu, Z.; Zhu, J.; Zhao, X. Efficiently activating peroxymonosulfate by CoFe-LDHs/MoS_2 for rapid degradation of tetracycline. *J. Water Process Eng.* **2023**, *53*, 103856. [CrossRef]
25. Yang, Z.; Li, X.; Huang, Y.; Chen, Y.; Wang, A.; Wang, Y.; Li, C.; Hu, Z.; Yan, K. Facile synthesis of cobalt-iron layered double hydroxides nanosheets for direct activation of peroxymonosulfate (PMS) during degradation of fluoroquinolones antibiotics. *J. Clean. Prod.* **2021**, *310*, 127584. [CrossRef]
26. Bai, R.; Yan, W.; Xiao, Y.; Wang, S.; Tian, X.; Li, J.; Xiao, X.; Lu, X.; Zhao, F. Acceleration of peroxymonosulfate decomposition by a magnetic MoS_2/$CuFe_2O_4$ heterogeneous catalyst for rapid degradation of fluoxetine. *Chem. Eng. J.* **2020**, *397*, 125501. [CrossRef]

27. Qiu, S.; Wang, Y.; Wan, J.; Ma, Y.; Yan, Z.; Yang, S. Enhanced electro-Fenton catalytic performance with in-situ grown Ce/Fe@NPC-GF as self-standing cathode: Fabrication, influence factors and mechanism. *Chemosphere* **2021**, *273*, 130269. [CrossRef]
28. Acharya, S.; Swain, G.; Parida, K. MoS_2-mesoporous $LaFeO_3$ hybrid photocatalyst: Highly efficient visible-light driven photocatalyst. *Int. J. Hydrogen Energy* **2020**, *45*, 11502–11511. [CrossRef]
29. Sanchez-Cupil, J.L.; Cuevas-García, R.; Guti, A.; Ramirez, J. The role of methoxy species on the transesterification reaction of castor oil on Ni-Mg-Al calcined hydrotalcites. *Catal. Today* **2022**, *392*, 31–40. [CrossRef]
30. Li, J.; Ma, W.; Zhong, D.; Li, K.; Ma, J.; Zhang, S.; Du, X. Oxygen vacancy concentration modulation of perovskite-based heterogeneous catalysts for Fenton-like oxidation of tetracycline. *J. Clean. Prod.* **2022**, *362*, 132469. [CrossRef]
31. Huang, H.; Guo, T.; Wang, K.; Li, Y.; Zhang, G. Efficient activation of persulfate by a magnetic recyclable rape straw biochar catalyst for the degradation of tetracycline hydrochloride in water. *Sci. Total Environ.* **2021**, *758*, 143957. [CrossRef] [PubMed]
32. Yang, Z.; Wang, Z.; Wang, J.; Li, Y.; Zhang, G. Facet-dependent activation of oxalic acid over magnetic recyclable Fe_3S_4 for efficient pollutant removal under visible light irradiation: Enhanced catalytic activity, DFT calculations, and mechanism insight. *Environ. Sci. Technol.* **2022**, *56*, 18008–18017. [CrossRef]
33. Li, J.; Zhong, D.; Huang, J.; Ma, W.; Li, K.; Li, M.; Wu, R.; Pu, C.; Wang, Q.; Zhou, Y. Cobalt mediated perovskite as efficient Fenton-like catalysts for the tetracycline removal over a neutral condition: The importance of superoxide radical. *Chemosphere* **2023**, *313*, 137564. [CrossRef]
34. Yan, Q.; Lian, C.; Huang, K.; Liang, L.; Yu, H.; Yin, P.; Zhang, J.; Xing, M. Constructing an acidic microenvironment by MoS_2 in heterogeneous Fenton reaction for pollutant control. *Angew. Chem. Int. Ed.* **2021**, *60*, 17155–17163. [CrossRef]
35. Feng, S.; Yu, M.; Xie, T.; Li, T.; Kong, D.; Yang, J.; Cheng, C.; Chen, H.; Wang, J. $MoS_2/CoFe_2O_4$ heterojunction for boosting photogenerated carrier separation and the dominant role in enhancing peroxymonosulfate activation. *Chem. Eng. J.* **2022**, *433*, 134467. [CrossRef]
36. Chen, P.; Gou, Y.; Ni, J.; Liang, Y.; Yang, B.; Jia, F.; Song, S. Efficient Ofloxacin degradation with Co(II)-doped MoS_2 nano-flowers as PMS activator under visible-light irradiation. *Chem. Eng. J.* **2020**, *401*, 125978. [CrossRef]
37. Luo, J.; Zhang, K.; Cheng, M.; Gu, M.; Sun, X. MoS_2 spheres decorated on hollow porous ZnO microspheres with strong wideband microwave absorption. *Chem. Eng. J.* **2020**, *380*, 122625. [CrossRef]
38. Wu, Y.; Li, Y.; He, J.; Fang, X.; Liu, J. Nano-hybrids of needle-like MnO_2 on graphene oxide coupled with peroxymonosulfate for enhanced degradation of norfloxacin: A comparative study and probable degradation pathway. *J. Colloid Interface Sci.* **2019**, *562*, 1–11. [CrossRef]
39. Zhou, J.; Liu, W.; Cai, W. The synergistic effect of Ag/AgCl@ZIF-8 modified g-C_3N_4 composite and peroxymonosulfate for the enhanced visible-light photocatalytic degradation of levofloxacin. *Sci. Total Environ.* **2019**, *696*, 133962. [CrossRef]

Disclaimer/Publisher's Note: The statements, opinions and data contained in all publications are solely those of the individual author(s) and contributor(s) and not of MDPI and/or the editor(s). MDPI and/or the editor(s) disclaim responsibility for any injury to people or property resulting from any ideas, methods, instructions or products referred to in the content.